

A Thesis Presented to
The Faculty of Alfred University

Thermoelastic Behavior of Al_2O_3 -SiC Nanocomposite via Microstructure-Based
Finite Element Analysis

by
Peter B. Hoskins

In Partial Fulfillment of
the Requirements for
the Alfred University Honors Program
May 1, 2017

Under the Supervision of:

Chair: Dr. David Lipke

Committee Members: Dr. Steven Tidrow, Dr. Darwyn Cook

Acknowledgements

I would like to thank my family for their generosity and support throughout my studies. I would also like to thank my advisor and committee for their tireless guidance and dedication during the project.

Contents

List of Figures	v
Abstract	v
Introduction	1
Nanocomposites and Residual Thermal Stress.....	1
OOF2 – Background	5
OOF2 – Analytical Modeling	7
Methods	9
Microstructure Generation.....	9
OOF2 Analysis	11
Results and Discussion	14
Conclusion	20
Future Work	20
References	22

List of Figures

Figure 1: Thermal loading near a particle.	Pg. 2
Figure 2: Stress field interactions on tangential stress.	Pg. 4
Figure 3: 2D hexagonal array of SiC particles in Al ₂ O ₃ and local tensile stresses along the intraparticle distance.	Pg. 4
Figure 4: Micrograph and periodic array of image, with coordinate system.	Pg. 10
Figure 5: Circular image with and without aliasing.	Pg. 10
Figure 6: Workflow diagram for OOF2 analysis.	Pg. 12
Figure 7: OOF2 mesh results.	Pg. 15
Figure 8: Close-up of interfacial region of skeleton.	Pg. 15
Figure 9: The hoop, or γ -component, of stress along the top edge boundary.	Pg. 16
Figure 10: Various values for stress up to the mean field distance within the matrix.	Pg. 17
Figure 11: Normalized stress along the top edge boundary.	Pg. 20

List of Tables

Table 1: Selected Properties of Al ₂ O ₃ and SiC.	Pg. 11
Table 2: Skeleton Parameters.	Pg. 13
Table 3: Hydrostatic Stresses Within SiC Particle.	Pg. 18

Abstract

In a composite material, thermomechanical behaviors of the constituent materials affect those of the final product. Near boundaries between the matrix and the reinforcement, stresses develop from temperature changes that affect the fracture toughness of the composite. Primarily, studies of these behaviors use either empirical results or mathematical analysis of geometric models. Here a model is developed within the OOF2 finite element program to replicate these particulate composites, specifically a ceramic matrix composite (CMC) of SiC in an Al₂O₃ matrix. Radial stresses were measured for the case of both a single particle in an infinite matrix and for multiple particles as the composite was subjected to a temperature decrease of 1000°C. The stresses as a function of radial distance and volume fraction of inclusion are compared against literature values. By establishing a base model, more complex analyses (e.g. multiple inclusion species, particle distribution effects) can be studied.

Introduction

Nanocomposites and Residual Thermal Stress

Nanocomposites are a class of materials that have been the subject of much interest primarily due to their mechanical behaviors, such as strength, the ability to withstand an applied load in an elastic manner (no permanent deformation), or toughness, the ability to absorb energy from deformation without fracture. For a composite reinforced with particles, stress distributions arise within the matrix under loading as a result of the reinforcement heterogeneities throughout the material. Because there is a difference in mechanical properties that relate stress and strain between the two materials, when loaded, will produce a residual stress distributed through the composite as long as the constituents remain bonded at their interface. Such a stress can arise with a mechanical load: if an external stress is applied, the respective stiffnesses of the constituents cause a strain mismatch. Under a temperature change, or thermal load, each material will produce a strain proportional to their coefficient of thermal expansion (CTE) and the amount of temperature change, resulting in a mismatch:

$$\varepsilon_{Thermal} = \Delta\alpha\Delta T \quad (1)$$

Experimentally, the relation has been shown by Brun and Singh in their study of shear stress due to thermal mismatch in ceramic matrix composites (CMCs)¹. For a variety of matrix compositions, they determined that if the fiber has a lower CTE than the matrix, shear stresses appear upon cooling, and increase linearly with the amount of mismatch.

Thermal loading is an important aspect to consider in the design of fabrication methods for composites that are formed above room temperature. At the forming temperature, there are no strains within the composite, as no temperature change has taken place. As it is cooled, the residual stresses and strains that develop may become large enough to satisfy failure criteria for one of the phases. By understanding the stress distributions in the composite, materials can be selected for a composite that will withstand a desired thermal load.

Selsing describes this, showing that the stress produced for the case of a single spherical particle in an infinite matrix is a function of each phases' Young's moduli, Poisson ratios, coefficients of thermal expansion, and also of the temperature change². This stress in the particle is a hydrostatic pressure (equal in all directions) and described by:

$$P = \frac{\Delta\alpha\Delta T}{\frac{1+\nu_m}{2E_m} + \frac{1-2\nu_p}{E_p}} \quad (2)$$

where E and ν are the Young's moduli or stiffness, and Poisson's ratio, respectively, of a particle and a matrix phase. To describe how the stress is distributed in the matrix, Selsing uses equations for stress in a thick-walled pressure vessel:

$$\sigma_r = \frac{R_i^3 P_i - R_o^3 P_o}{R_o^3 - R_i^3} - \frac{(P_i - P_o) R_i^3 R_o^3}{(R_o^3 - R_i^3) r^2} \quad \sigma_\theta = \frac{R_i^3 P_i - R_o^3 P_o}{R_o^3 - R_i^3} + \frac{(P_i - P_o) R_i^3 R_o^3}{(R_o^3 - R_i^3) r^2} \quad (3)$$

where r_i , r_o , P_i , and P_o are the inner radius, outer radius, inner pressure, and outer pressure of the vessel, respectively. As the limit of r_o is taken to infinity, the above expressions reduce to:

$$\sigma_r = -2\sigma_\theta = -P \frac{R^3}{r^3} \quad (4)$$

Figure 1 illustrates this relationship of stress as a function of radial distance.

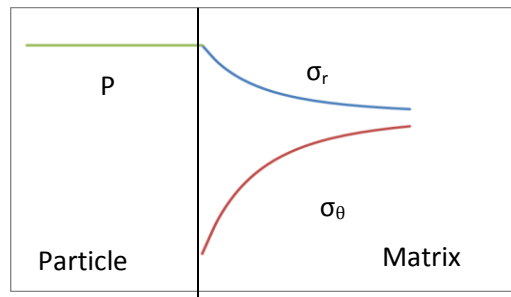


Figure 1. Stress distributions from thermal loading near a particle.

Ho and Suo demonstrate a similar relationship for a 2D case by assuming the geometry of a cylindrical instead of a spherical vessel³:

$$k = \frac{\frac{2E_m}{1+\nu_m}}{\frac{E_m}{1+\nu_m} + \frac{E_f}{1+\nu_f}} \quad (5)$$

$$\sigma = \frac{\Delta\alpha\Delta TE_f}{1-k\nu_f} \quad (6)$$

$$P = \frac{k\sigma}{2} \quad (7)$$

$$-\sigma_r = \sigma_\theta = P \frac{R^2}{r^2} \quad (8)$$

Taya et al. developed also a series of equations to determine average stress in both the particle and matrix⁴. The model differs from those of Selsing and Ho in that the system is not simply one inclusion within an infinite matrix, instead modeling some volume fraction of particles dispersed within a matrix phase:

$$\beta = \frac{1+\nu_m}{1-2\nu_p} \left(\frac{E_p}{E_m} \right) \quad (9)$$

$$\frac{\langle\sigma_p\rangle}{E_m} = \frac{-2(1-f_p)\beta\Delta\alpha}{(1-f_p)(\beta+2)(1+\nu_m)+3\beta f_p(1-\nu_m)} \quad (10)$$

$$\frac{\langle\sigma_m\rangle}{E_m} = \frac{2f_p\beta\Delta\alpha}{(1-f_p)(\beta+2)(1+\nu_m)+3\beta f_p(1-\nu_m)} \quad (11)$$

For the case of SiC in an alumina matrix, the average values of stress at the interface are about 1660 MPa when cooled from 1000°C. These values agree with a study of microstresses in the same composite when cooled from 1500°C performed by Levin⁵. The study measured volume fractions of inclusion ranging from 5-25%, and reported the principal stresses both in the matrix and in the reinforcement, with the stresses in the particle averaging approximately 1700 MPa compression.

However, when there are other particles near each other, the stress fields interact, and the stress does not fall completely to the full asymptotic value. The interaction of stress fields

from different particles is illustrated in a schematic adapted from Wang et al., shown in Figure 2, which illustrates how stress fields from nearby particles can affect stress distributions⁶. Near the particle interface, the contributions from other particles are minimal, and the stress distribution approximates that of a single particle in an infinite matrix.

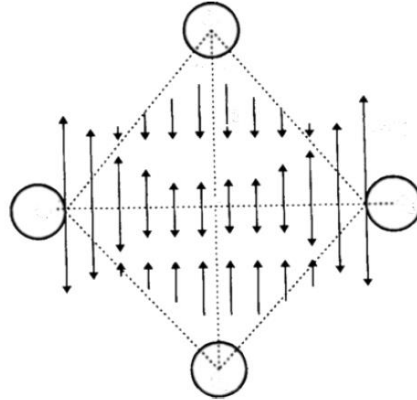


Figure 2. Schematic of the effect of stress field interactions on tangential stress.

Levin shows this effect in the case of a SiC- Al_2O_3 composite with SiC particles in a 2D hexagonal array⁷. In the paper, Levin assumed the presence of a crack propagating along the intragranular particle direction, and measured the stress perpendicular to that direction. The profile of the component of stress tangent to the surface of the particle, σ_y , along the intragranular particle distance decreases from approximately 800 MPa to below 200 MPa as shown in Figure 3b below. In this geometry, shown in Figure 3a, σ_y acts as a crack-opening stress as described by both the Griffith⁸ and Irwin⁹ models of crack growth.

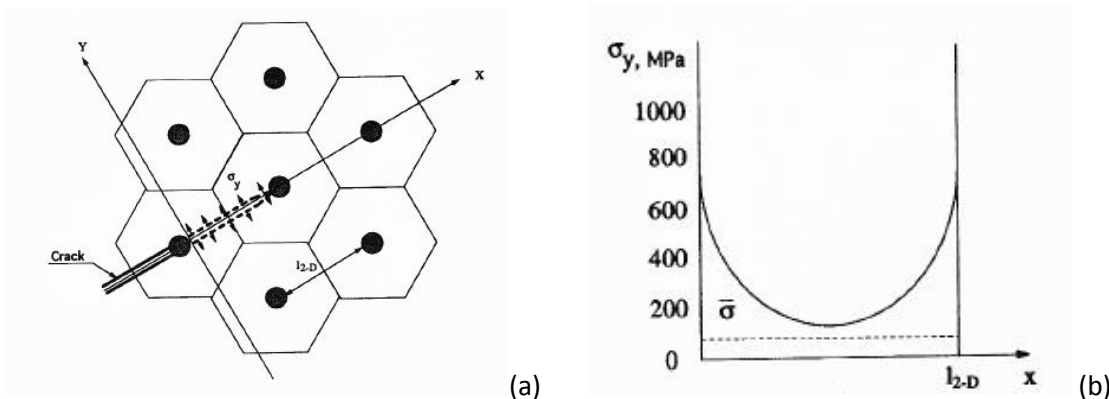


Figure 3. (a) Schematic for a 2D hexagonal array of SiC particles in Al_2O_3 . (b) Distribution of local tensile stresses along the intraparticle distance.

CMCs are favored in several industries for their performance in extreme conditions^{10, 11}. In particular, Al₂O₃ reinforced with SiC whiskers or particles has received significant attention for the possibilities of structural and machine applications¹²⁻¹⁴. Niihara et al. examined the mechanical properties of this particular composite at high temperatures. Specifically, they reported that when reinforced with SiC particulate, the fracture strength of the alumina matrix retained a value of 485 MPa even at temperatures of 1100°C¹⁵. This is a significant improvement over pure alumina, whose fracture strength is only 230 MPa at the same temperature. Ferroni and Pezzotti present evidence that this strengthening is caused by the presence of residual stresses within the composite¹⁶.

These composites are able to be processed in a variety of ways, some examples of which include spark-plasma sintering¹⁷, where internally generated heat from a DC current causes a precursor powder to sinter (coalesce and densify), sol-gel processing¹⁸, which involves dispersing SiC in boehmite sol, gelling, and sintering using gas pressure, and hot-pressing that utilizes external heat and pressure to densify powders into the final product¹⁹. These methods are able to achieve both fiber and particulate types of reinforcement with good microstructural control.

OOF2 – Background

In describing or determining the properties and responses of a material subject to some external condition, there are multiple methods to obtain data. Empirical analysis of a real material structure provides the most direct route to results, but requires preparation, equipment, and control of environmental variables/error. To complement experimental data and processes, computational methods provide twofold benefit: firstly, by investigating potential microstructures with a validated model, real-world experiments in synthesis of composites can be directed using predictive data, and secondly, by studying real-world structures using computational techniques, experimental computer-generated structures can be compared under similar conditions.

OOF2 is an object-oriented finite element (FE) software package originally developed by the National Institute of Standards and Technology (NIST) to perform analyses of linear elastic

two-dimensional microstructures²⁰. By importing a microstructural image and assigning parts of the image material properties, the software simulates the structure as it undergoes the effects of some fields: displacement, thermal, electrical, and others. OOF2 is used as one of several types of FE software in the field of composite science, some others being ABAQUS and ANSYS. OOF2 finds use where a multiple-component microstructure is either created by a script, or obtained by importing a micrograph of a material sample to serve as the microstructure. Thermomechanical models utilizing OOF2 are of special interest: by investigating the thermal contribution of the load, the beginnings of a purely thermal load case can be established.

Harry Chien et al. investigated residual thermal stresses resulting from ceramic coatings on a metal substrate, their variation with thickness, and the stress relaxation due to cracking²¹. In the paper, OOF2 is used to model the cross-section of the coating in order to examine the stresses with respect to the height, as with a laminar composite.

Tobias Ziegler et al. performed an analysis of AlSi12/ Al₂O₃ metal–ceramic composite with a lamellar microstructure²². In this case, the image was obtained from a micrograph of a surface perpendicular to the direction in which the sample was freeze-cast in the laboratory. The image retained the orientation of the lamellae with respect to the global axes, and was compared to other micromechanical models and ultrasonic phase spectroscopy. Here, the finite element analysis proves advantageous over mathematical models, as the complex lamellar structure does not lend itself as well to idealized or simplified assumptions used therein. OOF2 however is able to account for the non-uniform orientations present in the orientation map through direct computation. When compared to an inverse Mori-Tanaka model²³ and with the results of a spectroscopy analysis, the data was in good agreement with the empirical data, falling below both the modelled result and the mathematical fit. Such is expected, as both represent idealized structures. Ziegler also performed a similar analysis of these lamellae by dividing the orientations into poly-domains and determining the properties as they related to orientation²⁴.

An Al-SiC composite was analyzed using ABAQUS by Yu-Lin Shen in order to determine the composite temperature-dependent CTE for different cell structures – a Metal Matrix

composite (MMC), a CMC, and an interpenetrating cell composite²⁵. The three types of phase connectivity used temperature-dependent properties of each phase from 20°C to 600°C, with linear interpolation between data points. The CTE was output and compared to the volume fraction of SiC. For the MMC case, the trend line lies above the analytical upper bound without residual thermal stresses, while the CMC and interpenetrating cases lie between the bounds. With the residual thermal stress, each trend line lies between the two bounds. It is worth noting that the structure analyzed in the paper was not compared to any physical samples of Al-SiC.

Sharma et al. investigated how the effective Young's modulus of a Ni-Al₂O₃ CMC varied with the volume fraction of nickel²⁶. For both an interpenetrating composite and a particulate reinforced composite, analysis under a displacement field was carried out for volume fractions of 0.4, 0.6, and 0.8 Ni. The results were compared to ultrasonic measurements and both sets of data agree well. The authors comment that an advantage of OOF2 over other finite element packages is that because the image is used as an input, the boundaries of the structure do not need to be mathematically defined.

Vanessa Seriacopi et al. used OOF2 to analyze S290 steel under a pressure load, with a temperature ramp from room temperature to 1050°C and back²⁷. While not explicitly a composite, the steel does contain NbC as a second phase, and the resulting analysis shows that the two phases do indeed have different stress distributions as a result of heating, with stress distributions relaxing upon cooling to the pre-ramp temperature.

OOF2 – Analytical Modeling

For alumina/SiC composites, typical mathematical models regarding reinforcement of linear elastic materials hold well. The models of Selsing, Mori and Tanaka are commonly utilized, which evaluate effective properties from those of the constituents. Turner et al. described a different interpretation of the effective properties by examining deformation throughout the composite instead, with similar results and applications to those of Seriacopi²⁸.

A limitation of the OOF2 environment is the coordinate system in which the analyses are carried out. OOF2 makes use of only rectangular Cartesian coordinates to determine

distributions of fields, or to generate skeletons; polar coordinates are not supported by the program. As a result, analysis of fibers and particulates in composites as a radial cross-section requires a transformation in order to relate the output of Cartesian values into a polar reference. For hoop stresses in a ceramic, the coordinate transformation shown by W. Slaughter shows that as the angle θ approaches 0, the radial stresses disappear, and tangential stresses return to the form of stresses perpendicular to the radial direction i.e. σ_y ²⁹:

$$\begin{bmatrix} \sigma_x \\ \sigma_y \\ \sigma_z \end{bmatrix} = \begin{bmatrix} \cos^2\theta & -\sin^2\theta & 0 \\ \sin^2\theta & \cos^2\theta & 0 \\ 0 & 0 & 1 \end{bmatrix} \begin{bmatrix} \sigma_r \\ \sigma_\theta \\ \sigma_z \end{bmatrix} \quad (12)$$

$$\sigma_y = \sigma_r \sin^2\theta + \sigma_\theta \cos^2\theta \quad (13)$$

If the radial profile is coincident with the x-direction, as is the case in Figure 3, the radial stress can be equated to the x component of stress, and the tangential components to the y stress. This allows for modeling of particulate and fiber composites within OOF2.

To provide an effective model for any system using the finite element method, several factors must be considered. These include, but are not limited to, the quality of the geometry under analysis, the reliability of the boundary conditions applied, and successful convergence of the mesh. The latter factor is particularly important for cases in which there exist steep changes in fields across short lengths and accurate data in those lengths must be captured. Because each element in a mesh represents some portion of the material, by only using a few key points (nodes) for that volume element, some information is lost about the material response within that volume. This meshing effect decreases the accuracy of the results dramatically at low densities of elements. In order to balance the accuracy of a refined mesh using smaller volume element sizes relative to the model with the increased computing power required to solve the problems of the mesh, mesh convergence studies are frequently carried out in every FE package, including OOF2³⁰⁻³³. The goal of these studies is to approach some known data value or response. When an acceptable level of error is met, the mesh is kept at that desired resolution for use with further analyses.

Methods

Microstructure Generation

Before beginning an analysis with OOF2, a microstructural image was generated using Python code. The image consists of a rectangle containing black colored circles within a white field (Figure 4a). To prepare the image for a periodic boundary condition, the circles were generated such that their diameters or center points lay on either an edge or a corner of the image. The image is a rectangle with an aspect ratio of $2/\sqrt{3}$. The circles each have a radius of 21 pixels. This represents a 2D hexagonal array, with the picture edges as the short diagonals and side lengths of a hexagon. If the Figure was copied and tiled, the hexagonal array would appear (Figure 4b). In the image, the short side represents the intra-particle distance, a profile crossing the grain boundary connecting the two particles contained in the grains, as in Figure 3a.

When circular images are created using python code, at the edge of the circle aliasing is used to interpolate between the color of the circle and the color surrounding it. This serves primarily an aesthetic purpose, hiding from the viewer the pixel steps that approximate the curve of a circle and giving the illusion of true roundness. Aliasing is detrimental to use with OOF2 when assigning pixel groups via color, and as a result the was explicitly excluded from the image generation. The difference is shown in Figure 5.

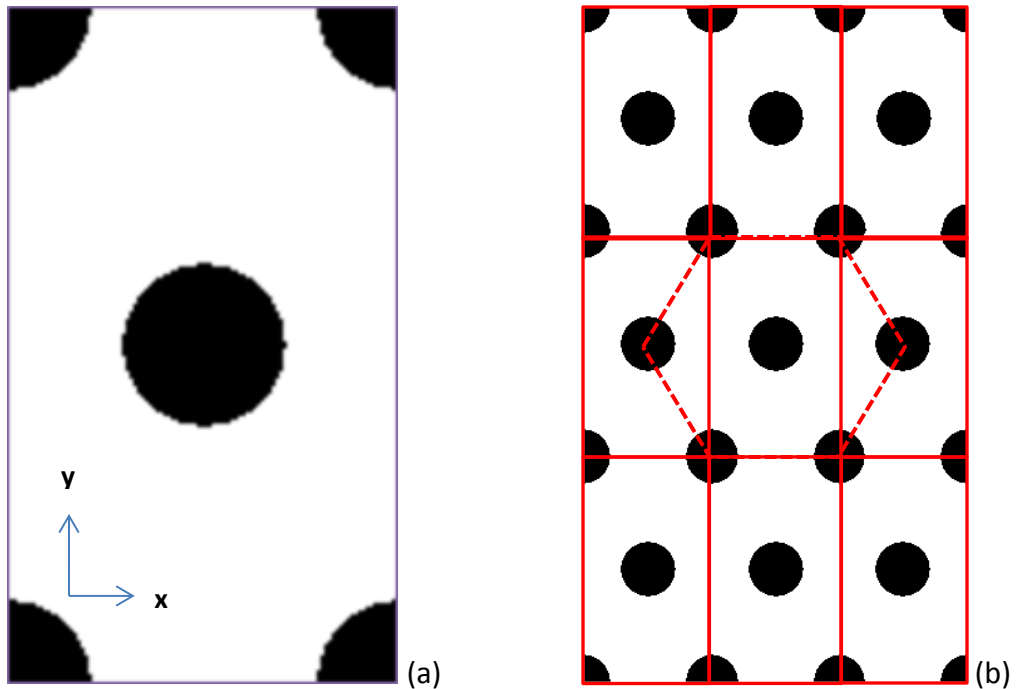


Figure 4. (a) Micrograph image, with coordinate system. (b) Periodic array of image, showing hexagonal arrangement.

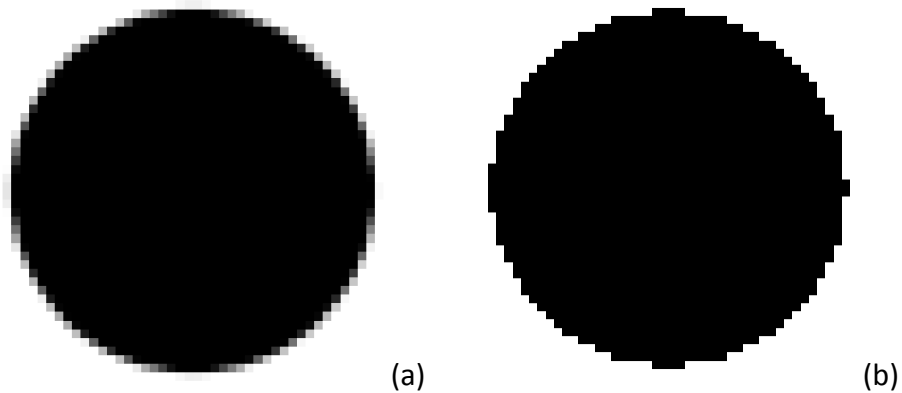


Figure 5. Circular image (a) with and (b) without aliasing.

To confirm that there remain no aliased or otherwise abnormally-colored pixels, a pixel count was performed via a color selection. All pixels of the same color were selected and counted. The count yielded a result of 15,644 pixels being colored white, and 2,896 being colored black, for a total of 18,540 pixels. This agrees with the dimensions of the image: $103 \times 180 = 18,540$; therefore, all pixels are accounted for. This represents a 6% volume fraction of

particles corresponding to 5 wt.% reinforcement. In addition, the boundaries were checked so that the top and bottom edges of the image had the same color pixels in the same locations along the edge. This was repeated for the right and left edges.

OOF2 Analysis

For the analysis, OOF2 version 2.1.12 was used. After generating microstructures, the analysis was carried out as shown in Figure 6, a workflow diagram for the analysis process in OOF2.

From the viewing window in OOF2, selections were made based on the color of the pixel: white pixels belonged in the matrix group and black pixels in the particle group. The removal of aliasing was necessary to remove the interpolated color region between the two sets of solid colors that did not belong to either group. Each pixel group was assigned three isotropic material properties: Young’s modulus E , Poisson’s ratio ν , and the coefficient of thermal expansion α . The values for each are based on data for SiC and Al_2O_3 ⁷, and are shown in Table 1. To maintain consistency with Levin, the materials were assumed to be isotropic (these materials are not isotropic in reality), reducing the number of parameters to 3.

Table 1: Selected Properties of Al_2O_3 and SiC.

Property	Al_2O_3	SiC
Young’s Modulus (GPa)	402	450
Poisson’s ratio	0.23	0.17
α ($^{\circ}\text{C}^{-1}$)	8.43	4.45

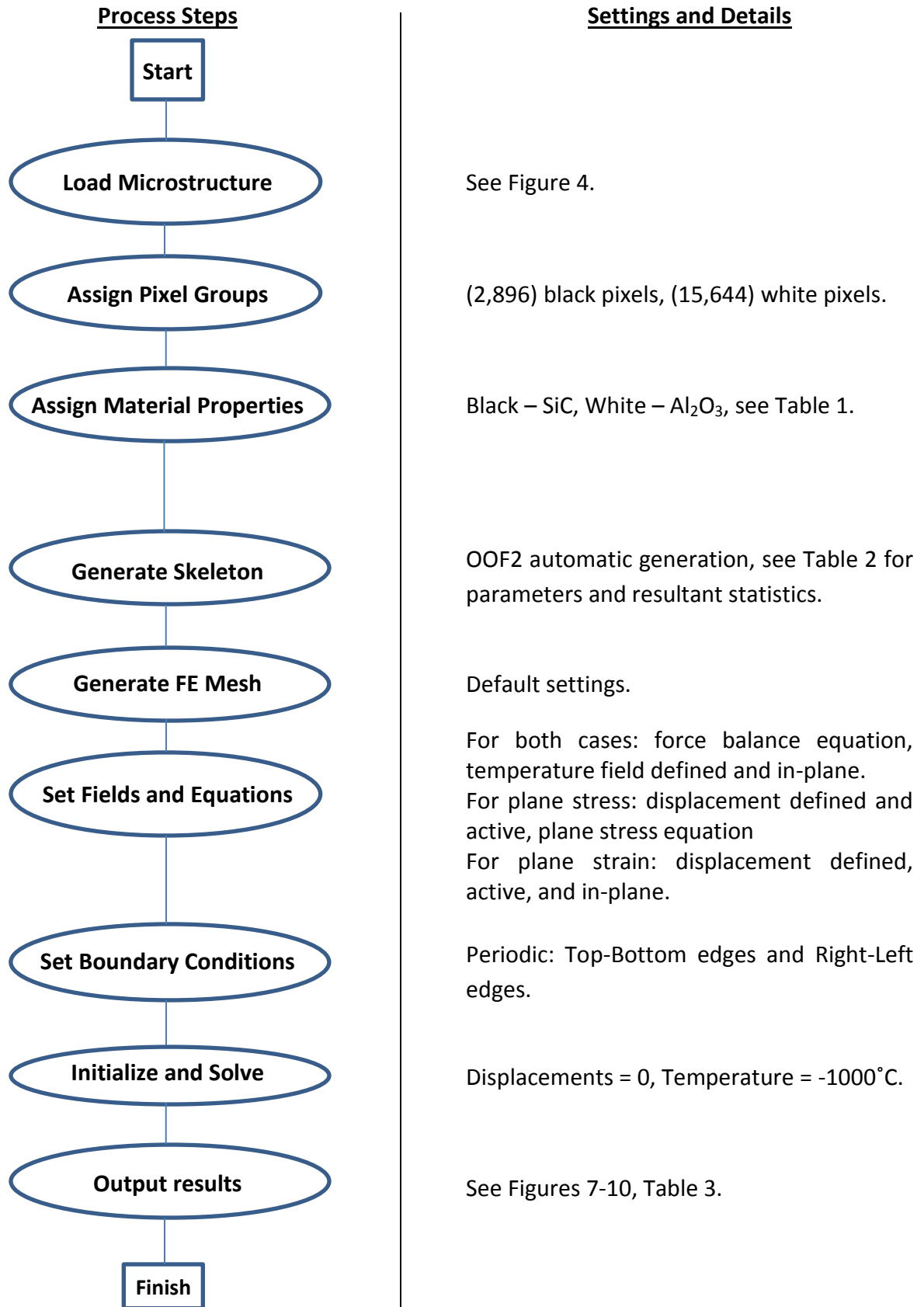


Figure 6. Workflow diagram for OOF2 analysis in the left column, with details and settings in the right column.

Before a finite element mesh can be generated, OOF2 requires the creation of a “skeleton” on which to lay the elements, a geometric object that represents the microstructure and is overlaid on top of it. After generating a skeleton that accurately represents the microstructure, a mesh can be generated that follows the geometry of the skeleton. The skeleton for each image was generated automatically. This process begins with overlaying a grid of elements on the microstructure, and then refining the skeleton through changes in the shape, size, and number of elements via bisection into smaller elements. The target when generating a skeleton is to have the length scale of the smallest elements fall below the minimum element size specified. The refinements are carried out only for elements that are insufficiently homogeneous, i.e. the element has too many pixels of differing groups. Other parameters of skeleton creation include the periodicity of the skeleton the maximum and minimum element size, and homogeneity index, a value identifying what percent of each skeleton’s elements must be of one group. The parameters for each case are shown in Table 2 below. By setting the skeleton as fully periodic, the nodes on one edge of the microstructure are treated as equivalent to the node at the same location on the side directly opposite it.

Table 2: Skeleton Parameters.

Maximum size (pixel)	5.0
Minimum size (pixel)	1.0
Homogeneity index	0.99
Number of elements	4501
Number of nodes	3089

A mesh was generated on the skeleton using the default parameters. For each case, there were two varieties of field/equation applied: plane-stress and plane-strain. The temperature field was defined and in plane but not set as active, and a force-balance equation was established. Periodic displacement boundary conditions were established on pairs of opposite sides. The initial conditions were set with all displacements being zero, and the temperature difference being -1000°C . The temperature difference is the difference between

the stress-free temperature $T_0=0^\circ\text{C}$, and the initialized temperature field $T = -1000^\circ\text{C}$. The system was solved with an iterative method, which works by solving the nodal system repeatedly, each iteration seeking to reduce the overall error in the system. For this analysis, the target for convergence to an answer was 10^{-13} error compared to a completely converged system.

After solving, the y-component of stress, or hoop stress, as shown in Figure 3 was plotted as a function of distance along the top edge of the mesh and output to a profile plot. The hoop stress profile along the intragranular distance was plotted, and hydrostatic stress within the particle was determined using Equations (2), (6), and (10) from the models of Selsing, Ho, and Taya, respectively.

Results and Discussion

The final mesh and outputs were generated as shown in Figure 7. The auto-refinement was primarily centered on the interface between the particle and the matrix, with refinements visible as shown in Figure 8. At a distance away from the interface equal to approximately 25% of the particle radius, the element size returns to the upper size limit. 51 of the 61 elements in the matrix phase along the top boundary were in an element at the max size, comprising 83.6% of those pixels.

For both the cases of plane stress and plane strain, three outputs were obtained and compared. The stress components directly output by the solver were collected in aggregate along the top edge of the skeleton, and the geometric strains were also collected along the same region. In the particle pixel group, the trace of the stress was output as an average value using the sampling points. OOF2 does not sample evaluations at nodes or at elements when using the analysis tool, instead providing options of either sampling by pixel, or by sampling of grid points. The sample creates a Cartesian coordinate grid with the origin at the lower left edge of the domain of the analysis – either a point boundary or a pixel group – and spaces out points in the x and y directions until the points overflow the domain. At every intersection on the grid, the desired output is measured. For the analysis, the grid spacing of both the x and y directions was 10 pixels.

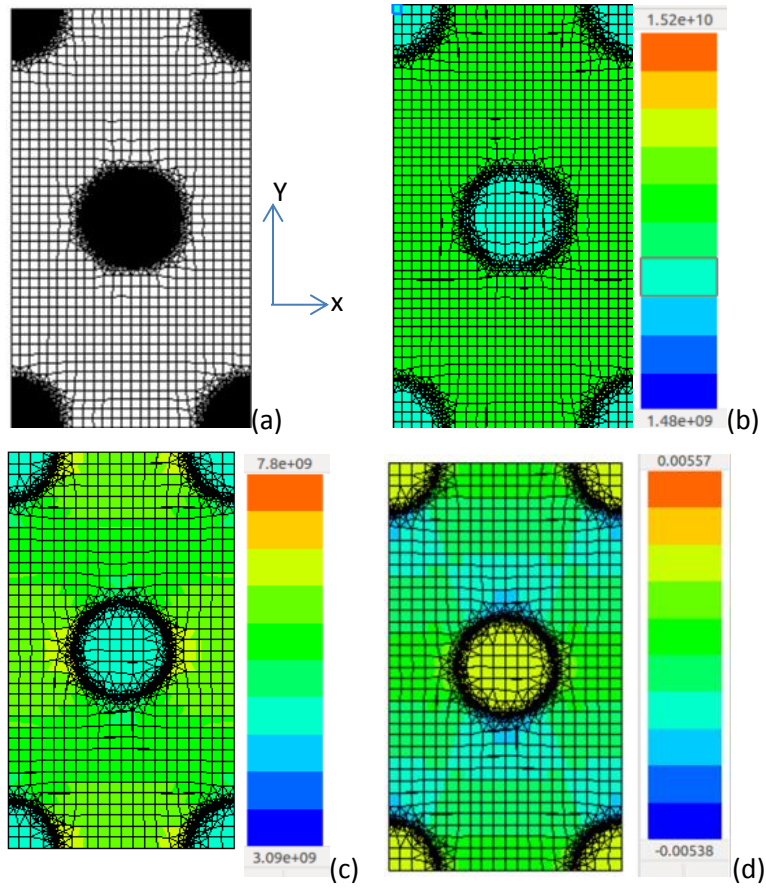


Figure 7. (a) Skeleton, (b) hydrostatic stress, (c) y-stress component, (d) y-strain component from OOF2 analysis. Stress in Pa.

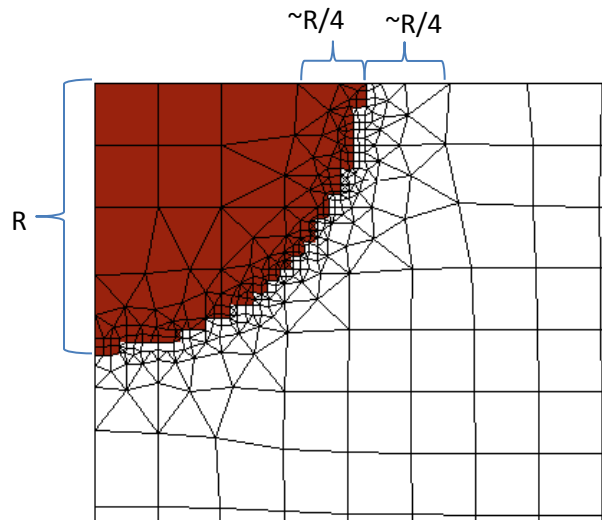


Figure 8. Close-up of interfacial region of skeleton. Refinement occurs at about +/- $\frac{1}{4}$ of the particle radius.

In an isotropic 3-dimensional or 2-dimensional material, stress and strain are related through a second order or first order-tensor rather than the zeroth order tensor (scalar) Young's modulus, as would be the case for a 1-D approximation. Through this relationship, a conversion from strain values to stress is developed, and is described for the case of the stresses by:

$$\sigma_y = \frac{(1-\nu_m)}{(1-2\nu_p)} (\varepsilon_y) E_m + \frac{(\nu_m)}{(1+\nu_m)(1-2\nu_m)} (\varepsilon_x + \varepsilon_z) E_m \quad (14)$$

Figure 2, shown below, illustrates the variation in the y-component of the stress along the entirety of the top edge boundary. The stresses within the particle are constant throughout the group, as expected; as stated earlier, Selsing describes a constant hydrostatic stress within an embedded particle, which implies that the components of the stress will also be constant throughout, agreeing with the shown trend. In addition, the stress within the matrix does decrease with distance away from the particle interface, reaching a minimum at the mean field between the two particles, i.e. halfway between them at a distance of 51.5 pixels.

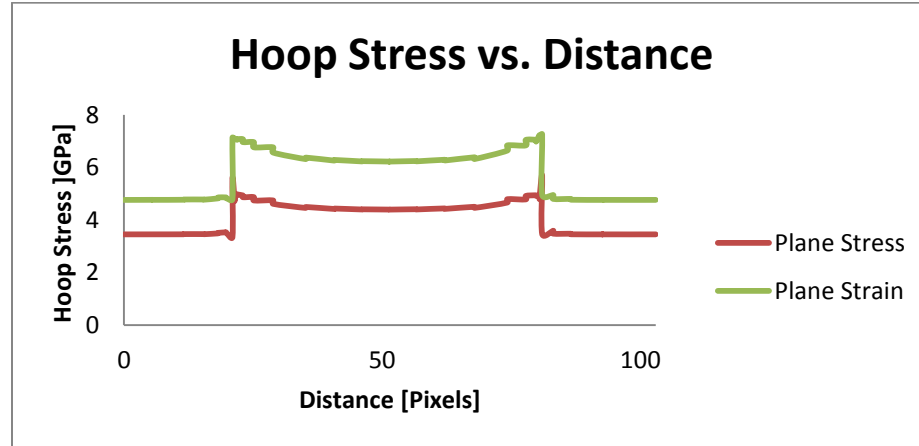


Figure 9. The hoop, or y-component, of stress along the top edge boundary.

The profiles of stress as obtained by direct output, conversion from an output strain, and as predicted by the analytic models introduced earlier, are gathered in Figure 10. These values are plotted against the normalized distance away from the interface, obtained by dividing the output distance along the boundary by the radius of the particle up to the mean-field within the matrix. The shapes of the output value profiles are caused by the nature of the

analysis: when evaluating the flux in the domain, values are reported for each node. Because nodes are connected by segments, two connected nodes have the possibility of showing the same value.

As can be seen, these figures elucidate several problems with the model as it stands. First, from the analytic models, the stress within the particle should be in compression along the studied boundary, and in tension within the matrix. However, for only one case analyzed did the stress in the matrix and the stress within the particles take values of different signs – the stress in the particle was observed to be positive. These results present an anomaly in trying to reconcile the stress distributions and balance of forces in the composite.

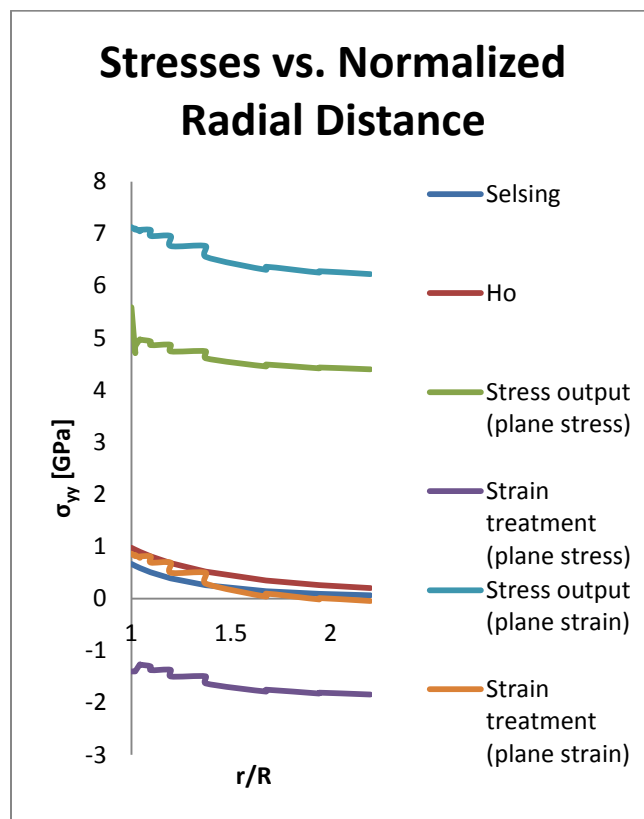


Figure 10. Various values for stress up to the mean field distance within the matrix.

Secondly, the profiles of stress along the chosen boundary differ greatly in magnitude from the predictive models. The magnitude difference occurs both along the matrix profile and along within the particle. Shown in Table 3 are the results of calculations of stress in the particle

for the models of Selsing, Ho and Suo, Taya, and Levin. The equations by which the values for the Selsing, Ho and Suo, and Taya models are obtained are given by equations (2), (5)-(7) and (9)-(10), respectively.

Table 3: Hydrostatic Stresses Within SiC Particle.

Model	Selsing	Ho and Suo	Taya	Levin	OOF2 (Plane Stress)	OOF2 (Plane Strain)
Hydrostatic Stress [MPa]	-1328	-974	-1290	-850	3454	4398

The variation of the model results cannot be explained simply from differences in assumptions made between the models in literature and those made during the creation of the micrograph image, namely that the image is of a reinforcement phase consisting of multiple particles as opposed to a singular inclusion within an infinite matrix. Plane stress and strain assumptions should in fact have an effect on the difference between the predicted and observed results, but mostly for the stress at distances far away from the interface where other stress fields contribute more to the resulting state of stress. At the interface, the observed stress should be in close agreement with that of the predictions. However, at the interface, i.e. $r/R = 1$, the stresses also significantly differ from those of the models. Some of the differences can be partially explained as consequences of the assumptions made within the model. For the conversion from strain under the plane stress assumption, Poisson effects result in a significant out-of-plane strain, about 3.5 times as large with opposite sign to make the second term in equation (14) to be larger than the first, and negative.

The anomaly cannot be explained simply by an error of high volume fraction either. By taking the observed average stress in the particle and comparing to the limits of volume fraction in Taya's model (Eq. (10)), as the volume fraction goes to 0, the upper limit of the stress

in the particle only approaches -1328 MPa, the value of Selsing's model, and is still far lower in magnitude than the observed results.

Notably, a normalization condition may be applied to the stresses in the profile. Such is performed by taking a particular point and finding the difference from the maximum value (occurring ideally at the interface), normalizing over the range of values. The resulting graph describes how the profiles decrease from the maximum value to their respective minimums as a function of radial distance. For all profile outputs, this normalization is collected in Figure 11. The trends when gathered show that, over the studied range, the magnitude falls off in a similar manner, and that there is some agreement between the models and the observed data.

The shape of the profile occurs due to the same reasons that cause the shape in Figure 10. There is error in the strain treatment for the plane stress condition in that the stress values at the interface were not the maximum on the evaluated interval. A significant observation of the results in the figure is that three of the outputs agree with each other for over 90% of the points: the direct output of stress under the plane strain condition, and the treatments of the output of strain for both the plane stress and plane strain conditions. This demonstrates that there is self-consistency within the analysis, and provides further evidence that the trends at least are approximate to the models, if not the true values.

From these observations, it can be gathered that the prominent obstacle in validating this model against the present literature is the issue of magnitude difference. This anomaly in the results has not been able to be ameliorated by any user-end adjustment of parameters within the OOF2 program. Without a thorough examination of the source code and its methodology for solving these types of simulations, it cannot be determined with certainty what aspect of the program may cause an error of this type, but some factors may be more significant than others in serving as a starting point for such an investigation. Such factors may include the method by which the program approaches problems utilizing the periodic boundary condition, as well as the method by which the stress flux is evaluated after the evaluation, or more generally how stress and strain are treated differently in the program: the former as a derivative of the field, and the latter as a flux of the field.

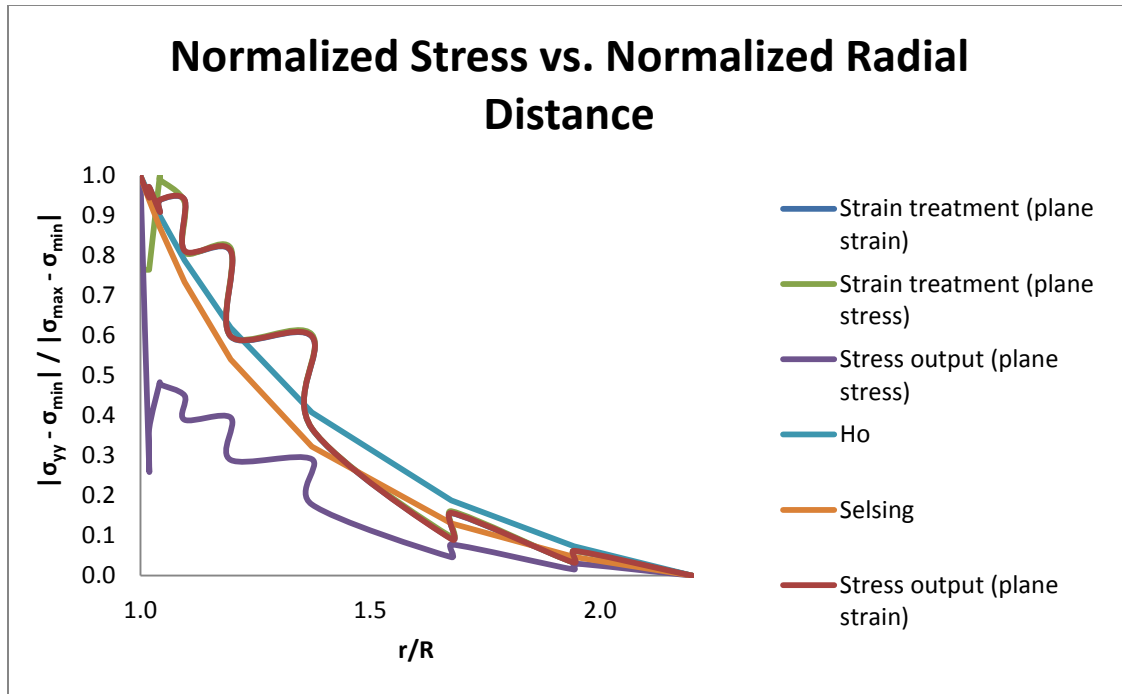


Figure 11. Normalized stress along the top edge boundary as distance from the particle interface increases. Profiles for strain treatments under plane stress and strain are coincident with that of the direct output of stress under plane strain.

Conclusion

A model of an $\text{Al}_2\text{O}_3\text{-SiC}$ nanocomposite from OOF2 was simulated, and the resulting thermal strains generated as a function of cooling were plotted against the normalized intragranular distance. In determining the stresses in the simulation, it was discovered that there exists an anomaly between the observed result and the predicted values for the system. Accounting for different assumptions, considerations and treatments, no satisfactory assessment of the source of the anomaly could be made, and the errors in the results of the analysis could not be addressed. As a consequence, the model as it stands cannot be properly validated, and is not useable as a representation of the $\text{Al}_2\text{O}_3\text{-SiC}$ nanocomposite system until the errors can be eliminated.

Future Work

To validate the model, the issue of magnitude difference must be resolved. The source of the issue may be attempted to be identified through two general methods: inspection of

code and adjustment of simulation conditions. Inspection of the source code requires an examination of the current problem and the algorithm by which it is addressed in OOF2, followed by a comparison to similar algorithms in alternative software packages. The assistance of the developers of the software at NIST may prove useful for such an endeavor, although it is not explicitly necessary in order to reach a solution.

Attempts to address the problem *in-situ* would primarily focus on testing the validity of OOF2's periodic boundary condition. This can be accomplished by the development of two microstructural images similar to the one created in this work, with adjustments made to the images. Instead of representing the microstructure with a single unit cell, the images would contain an aspect ratio, in terms of unit cell numbers. One would be a single cell long in the direction of the intergranular particle length, where the periodic boundary condition would be applied, and the other would be manually tiled to some number of unit cells long along the intragranular direction sufficient to approximate a periodic boundary condition; vice-versa for the other image. Stress distributions could be compared between the manually produced periodicity and the program-assumed periodicity to determine if there was a significant difference that was a result of only the change in definition of periodicity between the two images.

References

1. Milivoj K. Brun, "Effect of Thermal Expansion Mismatch and Fiber Coating on the Fiber/Matrix Interfacial Shear Stress in Ceramic Matrix Composites," *Adv. Ceram. Mater.* **3** [5] 506-09 (1998).
2. Jorgen Selsing, "Internal Stresses in Ceramics," *J. Am. Ceram. Soc.* **44** [8] 419 (1961).
3. S. Ho and Z. Suo, "Microcracks Tunneling in Brittle Matrix Composites Driven by Thermal Expansion Mismatch," *Acta Metall. Mater.* **40** [7] 1685-90 (1992).
4. Minoru Taya et al., "Toughening of a Particulate-Reinforced Ceramic-Matrix Composite by Thermal Residual Stress," *J. Am. Ceram. Soc.* **73** [5] 1382-91 (1990).
5. Igor Levin et al., "Residual Stresses in Alumina-SiC Nano-Composites," *Acta Metall.* **42** 1147-54 (1994).
6. Hongzhi Wang et al., "Analysis of the Residual Stress in Al₂O₃-SiC Nanocomposites," *Sci. China. Ser. E* **42** [3] (1999).
7. Igor Levin et al., "Effect of SiC Submicrometer Particle Size and Content on Fracture Toughness of Alumina-SiC 'Nanocomposites'," *J. Am. Ceram. Soc.* **78** [1] 254-56 (1995).
8. G.R. Irwin, "Linear Fracture Mechanics, Transition Fracture, and Fracture Control," *Eng. Fract. Mech.* **1** [2] 241-257 (1968).
9. A. A. Griffith, "The Phenomena of Rupture and Flow in Solids," *Philos. Trans. R. Soc. London, Ser. A* **221** 163-198 (1921).
10. S. Schmidt et al., "Advanced Ceramic Matrix Composite Materials for Current and Future Propulsion Technology Applications," *Acta Astronaut.* **55** [3-9] 409-420 (2004).
11. Hisaichi Ohnabe et al., "Potential Application of Ceramic Matrix Composites to Aero-Engine Components," *Composites Part A* **30** [4] 489-496 (1999).
12. *Synthesis and Properties of Advanced Materials*; Ch 9. P. 280. Edited by C.J. McHargue, J.B. Darby, Jr., Miguel José Yacamán, José Reyes Gasga. Kluwer Academic Publishers, Boston, MA, 1997.
13. Young Mok Ko et al., "Development of Al₂O₃-SiC Composite Tool for Machining Application," *Ceram. Int.* **30** [8] 2081-6 (2004).
14. Pankaj K. Mehrotra and William R. Huston, Kennametal PC Inc., "Whisker Reinforced Ceramic Cutting Tool and Composition Thereof," US. Pat. 9,399,071, March 2001.
15. K. Niihara et al., "High-Temperature Mechanical Properties of Al₂O₃-SiC Composites," pp. 103-116 in *Fracture Mechanics of Ceramics* Ch. 7. Springer US. 1986.
16. Luca Paolo Ferroni and Giuseppe Pezzotti, "Evidence for Bulk Residual Stress Strengthening in Al₂O₃/SiC Nanocomposites," *J. Am. Ceram. Soc.* **85** [8] 2033-38 (2002).
17. I. Álvarez et al., "Microstructural Design of Al₂O₃-SiC Nanocomposites by Spark Plasma Sintering," *Ceram. Int.* **42** [15] 17248-17253 (2016).
18. Unnikrishnan N. S. Hareesh, "Processing and Properties of Sol-Gel-Derived Alumina/Silicon Carbide Nanocomposites," *J. Am. Ceram. Soc.* **87** [6] 1024 (2004).

19. C. E. Borsa et al., "Processing and Properties of Al₂O₃/SiC Nanocomposites," *J. Microsc.* **177** [3] 305-312 (1995).
20. Rhonald Lua et al., "Modelling Microstructures with OOF2," *Int. J. Mater. Prod. Tec.* **35** [3/4] 361-73 (2009).
21. Chien et al., "The Influence of Residual Thermal Stresses on the Mechanical Properties of Multilayer α -Al₂O₃/TiC_xN_{1-x} Coatings on WC/Co Cutting Tools," *Surf. Coat. Technol.* **215** 119-26 (2013).
22. Ziegler et al., "Elastic Constants of Metal/Ceramic Composites with Lamellar Microstructures: Finite Element Modelling and Ultrasonic Experiments," *Compos. Sci. Technol.* **69** [5] 620-26 (2009).
23. T. Mori and K. Tanaka, "Average Stress in Matrix and Average Elastic Energy of Materials with Misfitting Inclusions," *Acta Metall.* **21** [5] 571-74 (1973).
24. Ziegler et al., "Multiscale Homogenization Models for the Elastic Behaviour of Metal/Ceramic Composites with Lamellar Domains," *Compos. Sci. Technol.* **70** [4] 664-70 (2010).
25. Yu-Lin Shen, "Thermal Expansion of Metal-Ceramic Composites: a Three-Dimensional Analysis," *Mater. Sci. Eng., A* **252** [2] 269-75 (1998).
26. Sharma et al., "Effective Young's Modulus of Ni-Al₂O₃ Composites with Particulate and Interpenetrating Phase Structures: a Multiscale Analysis Using Object Oriented Finite Element Method," *Comput. Mater. Sci.* **82** [1] 320-24 (2014).
27. Vanessa Seriacopi et al., "Multiscale Effect of Thermomechanical Loads on the NbC-Steel Microstructure Obtained by SPS," *Blucher Material Science Proceedings* **1** [1] (2014).
28. P. A. Turner et al., "Explicit Method for Calculating the Effective Properties and Micromechanical Stresses: an Application to an Alumina-SiC Composite," *Philos. Mag. A* **79** [6] 1379 (1999).
29. William S. Slaughter. *Linearized Theory of Elasticity*. Birkhauser, 2002.
30. Srinivasa R. Bakshi et al., "Computational Estimation of Elastic Properties of Spark Plasma Sintered TaC By Meshfree and Finite Element Methods," *Comput. Mater. Sci.* **50** [9] 2615-20 (2011).
31. Brandon A. McWilliams et al., "Probabilistic Response of Heterogeneous Particle Reinforced Metal Matrix Composites with Particle Size Dependent Strengthening," *Comput. Mater. Sci.* **79** 15-24 (2013).
32. S. Nadimi et al., "A Microstructure-Based Finite Element Analysis of the Response of Sand," *Paper presented at the Sixth International Symposium on Deformation Characteristics of Geomaterials, 15-11-2015 - 18-11-2015, Buenos Aires.* 816-23 (2015).
33. S. Nadimi et al., "A Microstructural Finite Element Analysis of Cement Damage on Fontainebleau Sandstone," *Paper presented at the ICTMS 2015, 2nd International Conference on Tomography of Materials and Structures, 29 Jun - 3 Jul 2015, Québec, Canada.* (2015).